water

MDPI

Article

Stripping of Cu Ion from Aquatic Media by Means of MgY_2O_4@g-C_3N_4 Nanomaterials

Abueliz Modwi [1,*], Hajo Idriss [2], Lotfi Khezami [3], Abuzar Albadri [1], Mukhtar Ismail [1], Aymen Amine Assadi [4,*] and Phuong Nguyen-Tri [5]

[1] Department of Chemistry, College of Science and Arts, Qassim University, Ar Rass 51921, Saudi Arabia
[2] Physics Department, College of Science, Imam Mohammad Ibn Saud Islamic University (IMSIU), Riyadh 13318, Saudi Arabia
[3] Chemistry Department, College of Science, Imam Mohammad Ibn Saud Islamic University (IMSIU), Riyadh 11623, Saudi Arabia
[4] National Center for Scientific Research (CNRS), National School of Chemistry of Rennes, University Rennes, ISCR—UMR 6226, 11 Allée de Beaulieu, 35700 Rennes, France
[5] Laboratory of Advanced Materials for Energy and Environment, University Du Quebec Trois-Rivieres (UQTR), 3351, C.P. 500, Trois-Rivieres, QC G9A 5H7, Canada
* Correspondence: ab.khalid@qu.edu.sa (A.M.); aymen.assadi@ensc-rennes.fr (A.A.A.)

Abstract: In this study, quaternary MgY_2O_5@g-C_3N_4 nanomaterials were produced using a simplistic ultrasonic power technique in the presence of an organic solvent, and their capability to abolish Cu (II) from an aqueous solution was evaluated. As validated by powder X-ray diffraction, the synthesized nanomaterials possessed excellent crystallinity, purity, and tiny crystalline size. According to BET and TEM, the nanomaterials with high porosity nanosheets and perfect active sites made Cu (II) removal from water treatment feasible. At a pH of 3.0, the MgY_2O_5@g-C_3N_4 displayed good Cu (II) adsorption capability. The Cu (II) adsorption adhered to the Langmuir adsorption model, with an estimated theoretical maximum adsorption aptitude of 290 mg/g. According to the kinetics investigation, the adsorption pattern best fitted the pseudo-second-order kinetics model. Depending on the FTIR results of the nanocomposite prior to and after Cu (II) uptake, surface complexation and ion exchange of Cu (II) ions with surface hydroxyl groups dominated the adsorption of Cu (II). The MgY_2O_5@g-C_3N_4 nanomaterials have great potential as adsorbents for Cu (II) removal due to their easy manufacturing process and high adsorption capacity. Additionally, the reuse of MgY_2O_4@g-C_3N_4 nanomaterials was tested through the succession of four adsorption cycles using HNO_3. The result showed the good stability of this material for mineral pollution removal.

Keywords: MgY_2O_4@g-C_3N_4 nanomaterials; Cu (II) ions adsorption; pH impact; sorption kinetics modeling

Citation: Modwi, A.; Idriss, H.; Khezami, L.; Albadri, A.; Ismail, M.; Assadi, A.A.; Nguyen-Tri, P. Stripping of Cu Ion from Aquatic Media by Means of MgY_2O_4@g-C_3N_4 Nanomaterials. *Water* **2023**, *15*, 1188. https://doi.org/10.3390/w15061188

Academic Editor: Wei Wei

Received: 16 February 2023
Revised: 15 March 2023
Accepted: 16 March 2023
Published: 19 March 2023

1. Introduction

Heavy metals are found everywhere in the natural world, and as human evolution has progressed; the possibility of being poisoned by metallic substances has increased [1]. This is because the body cannot process the remaining heavy metals, which are poisonous [2]. Industrial effluent contains several toxic metals, such as lead, chromium, copper, etc. Copper is a highly desirable metal that is widely used in several industrial applications including metal polishing, electricity, and metrological uses [3,4]. In recent decades, environmental knowledge of the problems presented by the release of copper-containing wastewater has developed in tandem with the quantity of copper-containing effluent from the electronics sector [5]. Furthermore, copper is a highly hazardous metal, even in small quantities. As per the U.S. Environmental Protection Act (USEPA), the highest permissible copper ions for industrial effluents are 1.3 mg/L whereas the World Health Organization recommends a concentration of no more than 2 mg/L for drinking water [6]. Thus, copper-contaminated

effluent should be cleaned prior to being released into the environment because of its toxic effects [3]. In recent years, various innovative strategies for removing copper ions from industrial effluents have been introduced, including adsorption, complexation, membrane filtering and electrocoagulation [7–9]. The adsorption of pollutants on the surfaces of adsorptive materials is an efficient technique for cleaning heavy metals [10,11]. Numerous materials, such as activated carbon, bentonite, and zeolite, are effective and competitive substances for use in heavy metal elimination from the aquatic environment [12–14].

Investigators have dedicated time and energy to invent suitable adsorption materials for removing heavy metals from wastewater [15]. Although these substances are economically affordable, we should develop methods to overcome their limitations, which are represented by their inefficiency and generation of secondary waste [16]. Recently, nanomaterials have drawn great interest for their exceptional ability to eradicate pollutants from the water system [17,18]. Enormous attempts have been made to manufacture nanocomposites with different properties by hybridizing and modification [19,20]. Different nanostructured materials exhibit several intriguing features, including particle size, mesoporosity, and large surface area [21,22]. Graphitic carbon nitride (g-C_3N_4) has emerged as an enticing research area, attracting wide multidisciplinary interest as a photocatalyst and environmental remediation material [23,24]. A g-C_3N_4 is a polymer composed of carbon and nitrogen atoms; it can be altered to change its surface properties without changing its composition and structure [25]. Because of the polymer characteristics of g-C_3N_4, its surface properties could be efficiently modified at the molecular scale through nanostructured materials [26]. In this work, for the first time to the best of our knowledge, we reported the synthesis of a MgY_2O_4@g-C_3N_4 composite by considering the synergistic advantage of the nontoxic MgO, Y_2O_3 oxide decoration on a g-C_3N_4 platform. Then, we demonstrated its application for the successful abolishing of Cu (II) ions from aqueous solutions, where we inspected the influence of different experimental conditions on Cu (II) ions removal, and conferred the plausible mechanism for the Cu (II) ions' interaction with the MgY_2O_4@g-C_3N_4.

2. Experimental Procedures

2.1. Preparation of MgY_2O_4@g-C_3N_4 Nanostructures

For MgY_2O_4@g-C_3N_4 nanosorbent, 0.011 moles of MgO and 0.002 moles of Y_2O_3 nanoparticles (Sigma Aldrich) were disseminated in 0.110 L of isopropanol for 0.40 h utilizing an ultrasonic bath. After adding 0.89 g of g-C_3N_4 nanosheet to the alcoholic solution, the mixture was sonicated for an additional 0.40 h at 500 rpm. The mixtures were then heated for 24 h at 75 °C in an electric drying oven, and the obtained nano-sorbent was ground prior to calcination. The resulting materials were then subjected to an annealing process lasting for 1.5 h at 145 °C as demonstrated in Scheme 1.

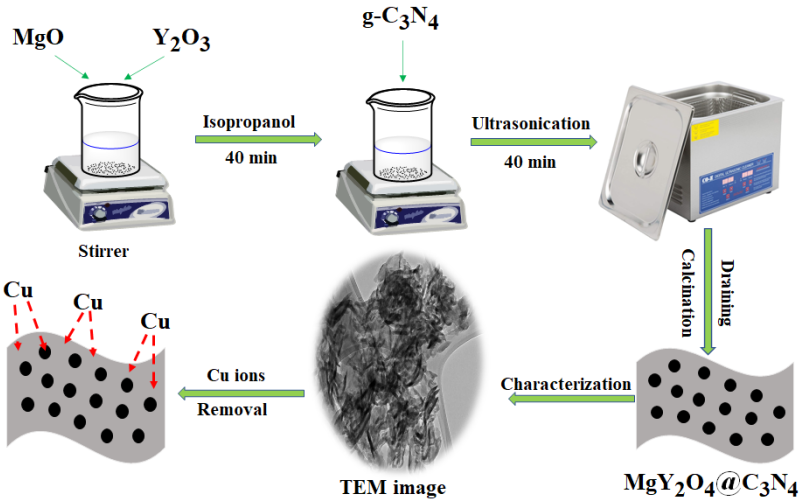

Scheme 1. Scheme of constructed of the MgY_2O_4@g-C_3N_4 nanocomposites.

2.2. Characterizations of MgY_2O_4@g-C_3N_4 Nanostructures

The crystallinity and structural features of MgY_2O_4@g-C_3N_4 nanocomposites were examined using an XRD system equipped with a Cu-K radiation source (λ = 1.5418 Å). The surface area of the nanocomposite was estimated by N_2 adsorption/desorption at 196 °C using a Micro-metrics ASAP 2020 analyzer (Norcross, Georgia, USA). A transmission electron microscope (TEM) combined with electron dispersive X-ray (EDX) spectrometry was utilized for morphology and elemental composition identification. X-ray photoelectron spectroscopy (XPS) was used to probe the synthesized nanomaterials surface chemistry. FTIR was employed to study the variations of MgY_2O_4@g-C_3N_4 nanomaterials functional groups before and after Cu (II) elimination.

2.3. Cu (II) Adsorption Test

The isotherms for Cu (II) adsorption on MgY_2O_4@g-C_3N_4 nanohybrid were examined in batch experiments. In 0.025 L glass vials, 10 mg MgY_2O_4@g-C_3N_4 was added to Cu (II) at various concentrations from 5 to 200 ppm. The solution was stirred continuously for 24 h. After equilibrium was attained, the nanocomposite was filtered, and atomic absorption spectroscopy was used to quantify Cu (II) concentrations. The quantity of Cu (II) ions adsorbed at any given time and consequent equilibrium magnitudes q_t and q_e were computed utilizing Formulas (1) and (2).

$$q_t = \frac{1}{m}(C_0 - C_t)V \quad (1)$$

$$q_e = \frac{1}{m}(C_0 - C_e)V \quad (2)$$

where the terms V, C_0, C_e and C_t stand the solution volume (L), initial concentration, equilibrium concentration, and concentration at time t of Cu (II) metal ions (mg/L) in solution, and m the adsorbent's mass (g). The average of triplicate measurements was taken. The regeneration experiment was conducted according to [9] where the solution after Cu (II) ions adsorption adsorbent was filtered to separate the adsorbent, washed three times with de-ionized water, soaked in diluted HNO_3 and finally filtered after shaking at 300 rpm for 60 min. Then, the adsorbent was washed with deionized water and left to dry at 80 °C for 15 h before performing the next adsorption cycle.

The Freundlich [27], Langmuir [28], Dubinin–Radushkevich [29], and Temkin [30] numerical methods were applied to the experimental analysis to determine the adsorption equilibrium mechanism of the adsorbent.

$$q_e = K_F C_e^{1/n} \quad (3)$$

$$q_e = \frac{Q_{max} K_L C_e}{1 + K_L C_e} \quad (4)$$

$$q_e = q_m e^{-K\varepsilon^2} \quad (5)$$

$$q_e = q_m exp\left(-\beta\varepsilon^2\right) \quad (6)$$

The isotherm of Cu (II) adsorption on MgY_2O_4@g-C_3N_4 nanomaterials was examined via adding a specified quantity of adsorbent (10 mg) to a Cu (II) solution (5 to 300 mg/L) at room temperature for 1440 min.

Identifying the adsorption kinetics characteristics of the sorbent is essential in the environmental remediation of heavy metals [31]. Thus, Pseudo-first order (PFO), pseudo-second order (PSO), and intra-particle diffusion models (IPD) were used to analyze the adsorption of Cu (II) ions on MgY_2O_4@g-C_3N_4 nanomaterials. The three nonlinear mathematical models used in this study are given in equations below.

Kinetics Model	Equation		Plots	Ref.
Pseudo-first-order	$q_t = \left(q_e - e^{-k1t}\right)$	(7)	$q_t\ vs\ \ t$	[1]
Pseudo-second-order	$q_t = \frac{q_e^2 k_2 t}{1 + q_e k_2 t}$	(8)	$q_t vs\ t$	[2,3]
Elovich	$q_t = \frac{1}{\beta} \ln(1 + \alpha\beta t)$	(9)	$q_t\ vs\ \ t$	[4]
Intra-particle Diffusion	$q_t = k_{dif} t^{1/2} + C$	(10)	$q_t\ \ vs\ \ t^{1/2}$	[5,6]
Mass Transfer	$Ln(C_0 - C_t) = Ln(D) - \ k_0 \cdot t$	(11)	$Ln(C_0 - C_t)\ vs\ t$	[5,6]

3. Results and Discussions

3.1. MgY_2O_4@g-C_3N_4 Nanomaterial Structural Analysis

As illustrated in Figure 1a, the XRD pattern of MgY_2O_4@g-C_3N_4 nanomaterials indicates sharp diffraction peaks with comparative widening and intensities, indicating the production of a well-nano-crystallized phase. Employing the High Score instrument to identify peaks demonstrates the existence of MgO, Y_2O_3, and g-C_3N_4 phases. The g-C_3N_4 nanosheet diffraction peaks at 2θ = 12.84° and 27.36° match with the in-plane structural contents pattern (100) and interlayer stacking plane (002) of the hexagonal structure (JCPDS card No. 87-1526) [32]. The different peaks observed at 2θ of 36.72°, 42.84°, and 61.84° are assigned to the (111), (200), and (220) planes of the MgO cubic symmetry [33]. Besides the peaks 20.30, 29.31, 33.74, 39.72, 48.41, 53.02, and 57.51° correspond to the (211), (222), (400), (332), (440), (611) and (622) Miller indices of pure body-centered cubic Y_2O_3, respectively (JCPDS No. 41-1105) [34].

A suitable adsorbent, such as MgY_2O_4@g-C_3N_4 nanoparticles, must have a substantial number of adsorption sites. In other words, the material's surface area, pore-volume, and size should be sufficient. The nitrogen adsorption-desorption investigation (Figure 1b) demonstrates that MgY_2O_4@g-C_3N_4 nanoparticles are a mesoporous material with an IUPAC type IV adsorption isotherm. The isotherm is associated with a type H1 hysteresis, suggesting a confined distribution of homogeneous mesoporous and inflexible networking impacts [35,36]. MgY_2O_4@g-C_3N_4 nanomaterials have a surface area, total porous volume, and average pore size of 90.51 m^2/g, 0.356 cc/g, and 2.53 nm, respectively. It is anticipated that the adsorbent's huge surface area and porosity will expose a significant number of adsorption sites, leading to high adsorption efficiency.

TEM images of the produced MgY_2O_5@g-C_3N_4 nanomaterials revealed two-dimensional nanosheet-like nanoparticles, as publicized in Figure 1c–e. The combined MgO and Y_2O_3 nanoparticles in the MgY_2O_5@g-C_3N_4 nanomaterials exposed a particle with an average size between 20 and 50 nm, as observed. The EDX spectrum (Figure 1e) reveals recognizable Y, Mg, N, O, and C peaks, thus verifying the purity of the produced composite. In addition, the composition of C, N, O, Mg, and Y, as depicted in Figure 1f, clearly demonstrated the homogenous distribution of the elements across the examined particles.

XPS was employed to examine the surface chemical composition of MgY_2O_5@g-C_3N_4 nanomaterials, as well as the interaction between g-C_3N_4 and Y_2O_3 and MgO. The XPS survey spectra and high resolution XPS spectra of the O 1s, Y 3d, Mg 2p, C 1s and N 1s areas are shown in Figure 2. The survey spectra (Figure 2a) revealed the presence of C, N, O, Y, and Mg on the surface of MgY_2O_5@g-C_3N_4 nanomaterials. The narrow O 1s peaks in Figure 2b may be deconvoluted to three peaks with binding energies of 530.64, 532.36, and 533.90 eV, which correspond to the lattice oxygen of the layer-structured Y_2O_3, and/or MgO and adsorbed H_2O or surface hydroxyl oxygen, respectively [37]. The three primary peaks in Figure 2b, at 157.96 eV, 159.11 eV, and 160.25 eV, respectively, reflected the Y3d for Y metal and (3d5/2 and 3d3/2) of stoichiometric Y_2O_3 oxide [38,39]. The signal at 51.45 eV in the Mg XPS spectrum (Figure 2c) might be attributed to the distinctive Mg 2p peak for MgO [23]. Figure 2e shows the high-resolution C 1s spectrum, which features two distinct contributions at 284.97 and 287.60 eV, which are attributed to carbon in the C-C and C=N/C=O states, respectively [40,41]. Figure 2f shows a high-resolution N 1s spectra with three distinct peaks centered at 398.27, 400.41, and 404.17 eV, which were attributed to the

pyridine N, pyrrolic N, and graphitic N, respectively [42], indicating that the MgY_2O_5@g-C_3N_4 nanomaterials surface was rich in nitrogen-containing functional groups.

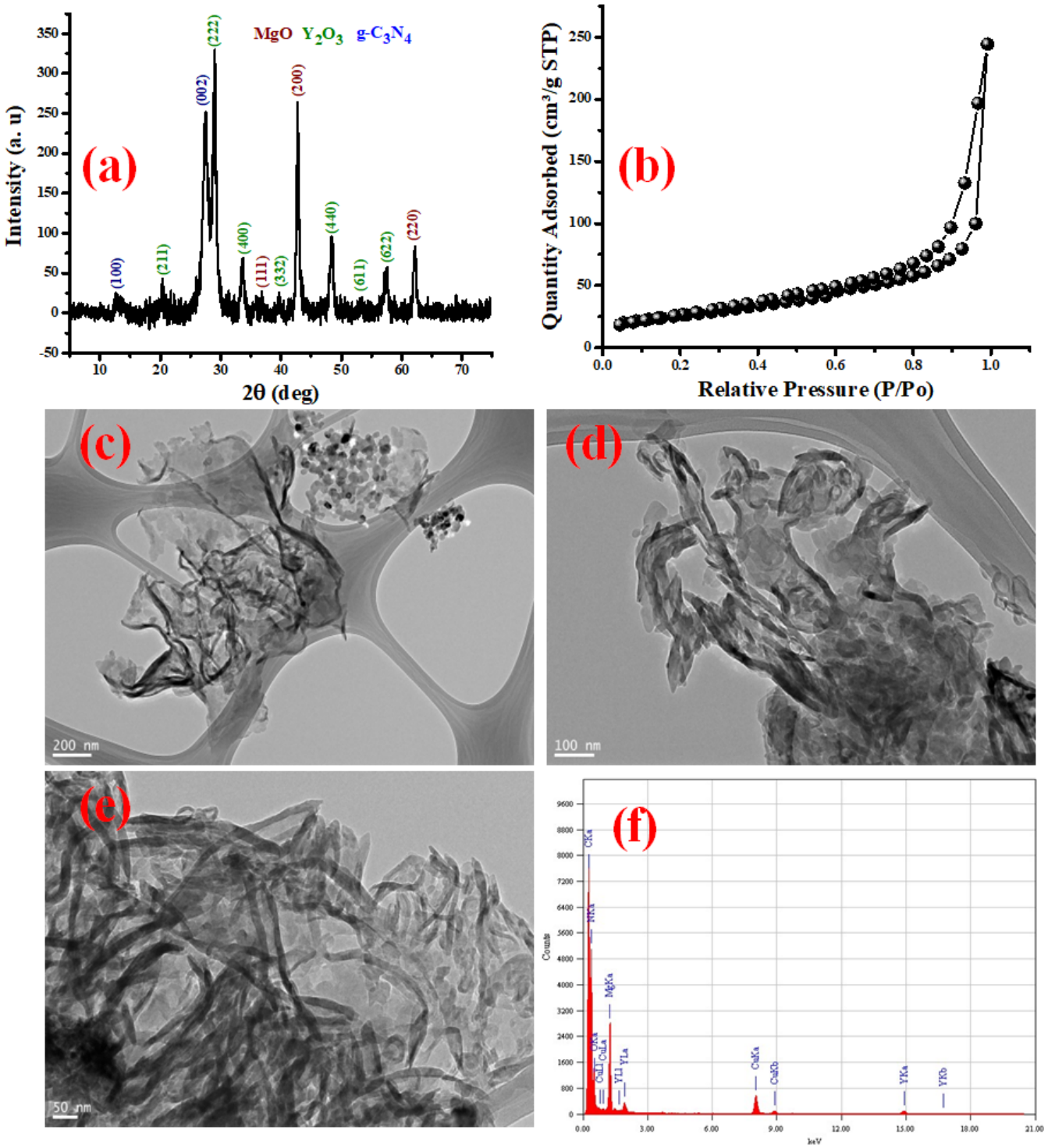

Figure 1. (**a**) XRD pattern; (**b**) BET surface area graph; (**c**–**e**) TEM images with different magnifications; and (**f**) EDX of MgY_2O_4@g-C_3N_4 nanomaterials.

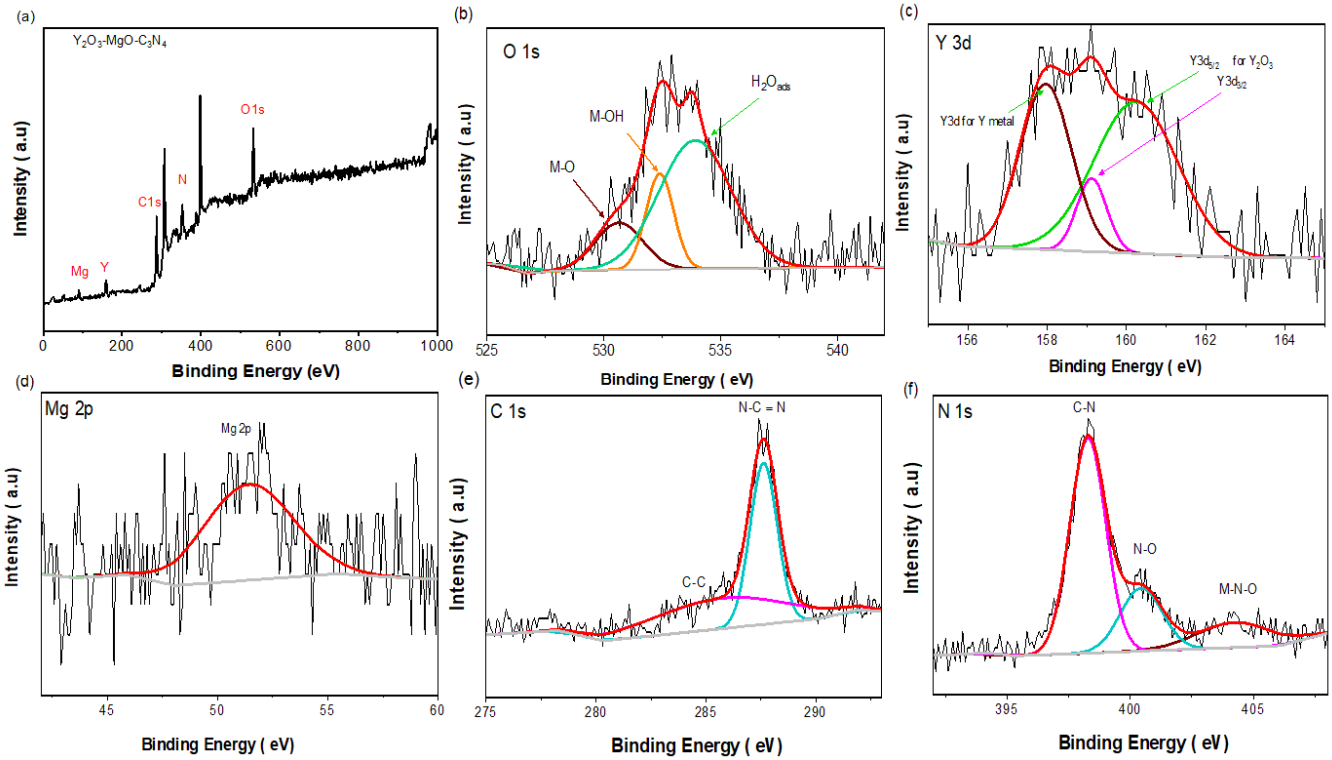

Figure 2. XPS spectra of (**a**) survey; (**b**) O 1s; (**c**) Y 3d; (**d**) Mg 2p; (**e**) C 1s; and (**f**) N 1s for Y_2O_3-MgO@g-C_3N_4 nanocomposite.

3.2. Cu (II) Removal onto MgY_2O_4@g-C_3N_4 Nanomaterial

3.2.1. Effect of Cu (II) Initial Concentration

The impact of Cu (II) concentration was evaluated over a wide concentrations range (5 to 300 mg/L) within ideal operating conditions. These conditions comprised 10 mg of MgY_2O_4@g-C_3N_4, with a constant volume of Cu (II) (25 mL), room temperature, and a 24-h contact duration. The Figure 2 shows the variation of adsorption capacity as function of Cu (II) initial concentration by MgY_2O_4@g-C_3N_4 nanomaterials. Figure 3 depicts the percentages and optimal adsorption capacity of Cu (II) on MgY_2O_4@g-C_3N_4 sorbent. It can be observed that when the concentration of Cu (II) rises, the adsorbed amount also rises steadily from 9.85 to 250 mg/g. In this particular scenario, the primary driving force that rise in the initial Cu (II) concentration surmounted any impediment to Cu (II) movement from the solution [26]. Because of this, the fractional adsorption produced is directly proportional to the concentration. This behavior is similar to that obtained with Tran and his coworkers in the case of the removal of Pb (II) from aqueous media by a new design of Cu–Mg binary ferrite [36].

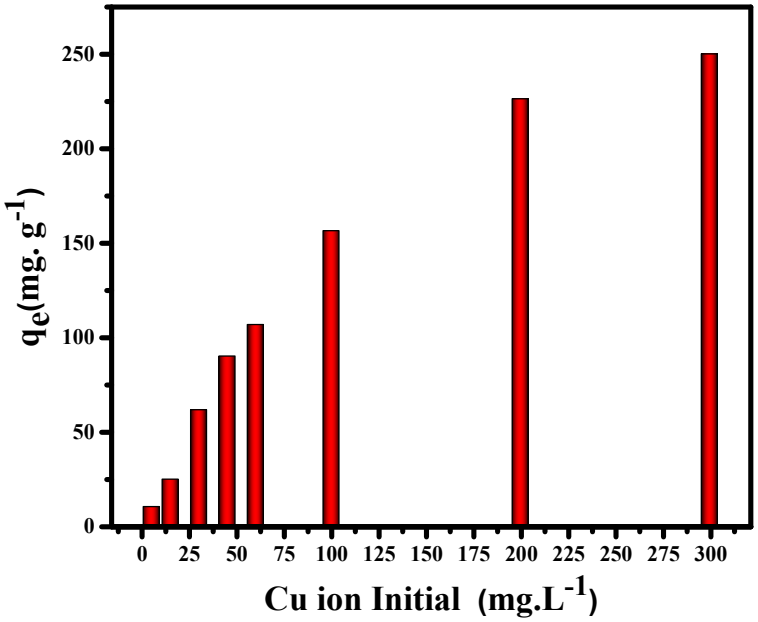

Figure 3. Variation of adsorption capacity of Cu (II) with the initial concentration (conditions: 25 °C; adsorbent dosage: 10 mg; stirring speed: 400 rpm; contact time: 24 h; initial Cu (II) concentration: 5–300 mg/L, pH = 7).

3.2.2. Cu (II) Removal and pH

The pH level is critical for realizing the rate of surface reactions between adsorbate (Cu (II)) and MgY_2O_4@g-C_3N_4 sorbent. An investigation of the impact of pH on Cu^{2+} adsorption has been conducted from pH 1.0 to 8.0. Figure 4 highlights the influence of pH on adsorption capacity (mg·g^{-1}) of Cu ions where a maximum value was measured at pH 3. Adsorbate-adsorbent interactions decrease below pH = 3 because protonation takes place on the sorbent surface. A competition between H^+ and the positively copper ions for the available active sites at the adsorbent's surface rationalizes the reduced Cu ion adsorption at low pH values. These findings are in agreement with those reported in other studies [43]. Cu (II) has a pH dependence on its solubility as it exists as soluble free ions and Cu $(OH)^+$ at lower pH levels. Moreover, Cu (II) ions tend to precipitate as copper hydroxides ($Cu(OH)^0_2$, $Cu(OH)_3{}^-$, and $Cu(OH)_4{}^2$) above pH 7 [8]. Based on these findings, the quantitative Cu (II) ions elimination ability decline with the pH increase until it reaches a minimum value at pH = 8.

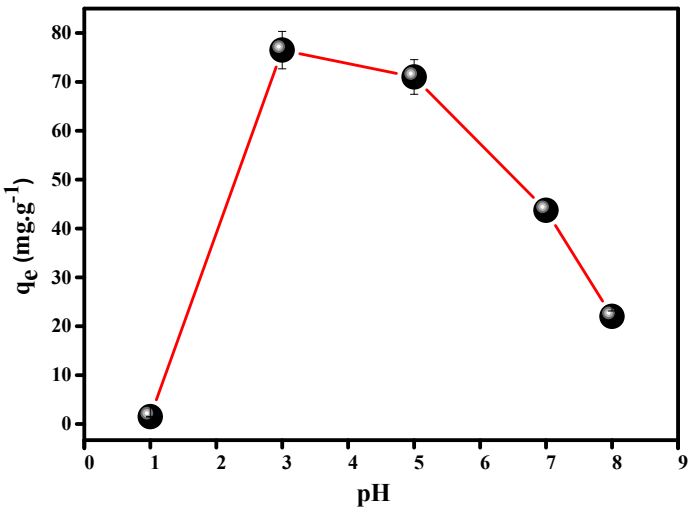

Figure 4. pH dependence of the adsorption capacity (mg·g^{-1}) of Cu ions.

This behavior is similar to that obtained by Tran and his coworkers in the case of the removal of Pb (II) from aqueous media by a new design of Cu–Mg binary ferrite [36].

3.2.3. Cu (II) Elimination and Equilibrium Contact Time

The adsorption of 45 mg/L Cu (II) ions initial concentration on MgY_2O_4@g-C_3N_4 nanosorbent was examined for periods of 0 to 1440 min as illustrates in Figure 5. In less than 40 min, the elimination of Cu (II) against the contact time reaches equilibrium. According to several active sites on the MgY_2O_4@g-C_3N_4 surface, the Cu (II) sorbed quantity achieves around 86.65 mg/g. At equilibrium, the quantity of the active site normally declines, and the exclusion percentage stabilizes to a steady level. It is anticipated that the adsorbent's vast surface area and porosity will avail a huge sum of adsorption sites, leading to enhanced adsorption efficiency [44].

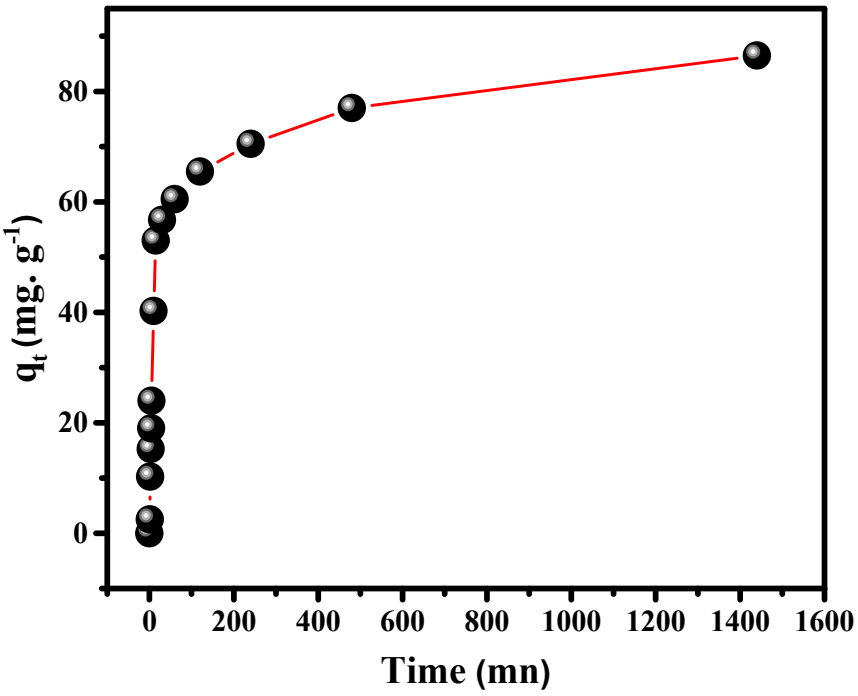

Figure 5. Impact of interaction time on the Cu (II) ions sorption onto MgY_2O_4@g-C_3N_4.

3.2.4. Adsorption Isotherms Modeling

According to the initial concentration of 5 mg/L, the equilibrium concentration of Cu (II) is determined to be 9.5 mg/g, leading to an elimination rate higher than 99% (Figure 6 and Table 1). This result demonstrates that MgY_2O_4@g-C_3N_4 is powerful in Cu (II) adsorption.

The Freundlich model parameters K and n are correlated to the bond force and dispersion. The Langmuir model defines q_{max} as the level of solid-phase encasement of all monolayer adsorption zones (Equation (4)). K_L is associated with the adsorption free energy. For the Langmuir: the feature of the sorbent is uniform; the adsorbed molecules or atoms are kept in separate and stable sites, and each location may accommodate just one molecule or atom. The adsorption energy is constant among all parts, and there is no interplay between bordering adsorbent surfaces and adsorbed molecules. Comparatively, the Freundlich model deals with non-homogeneous systems and reversible adsorption; however, monolayer adsorption is not restricted. Figure 6a–d displays graphs of experimental values modeled via Langmuir, Freundlich, Temkin and Dubinin–Radushkevich. The Langmuir model demonstrates a superior matching with the data with (R^2 = 0.9965) compared to R^2 = 0.9644 for the Freundlich model (Figure 6b). The Langmuir model (Figure 6a) reveals that the highest adsorption capacity of the MgY_2O_4@g-C_3N_4 is 290.7 mg/g. The high capacity of the nanomaterial is owing to its improved surface area and large pores [45].

This observation indicates that Cu (II) ions are captured as monolayers on the MgY_2O_4@g-C_3N_4 surface by chemisorption, which is the predominant mechanism of the Langmuir model [46].

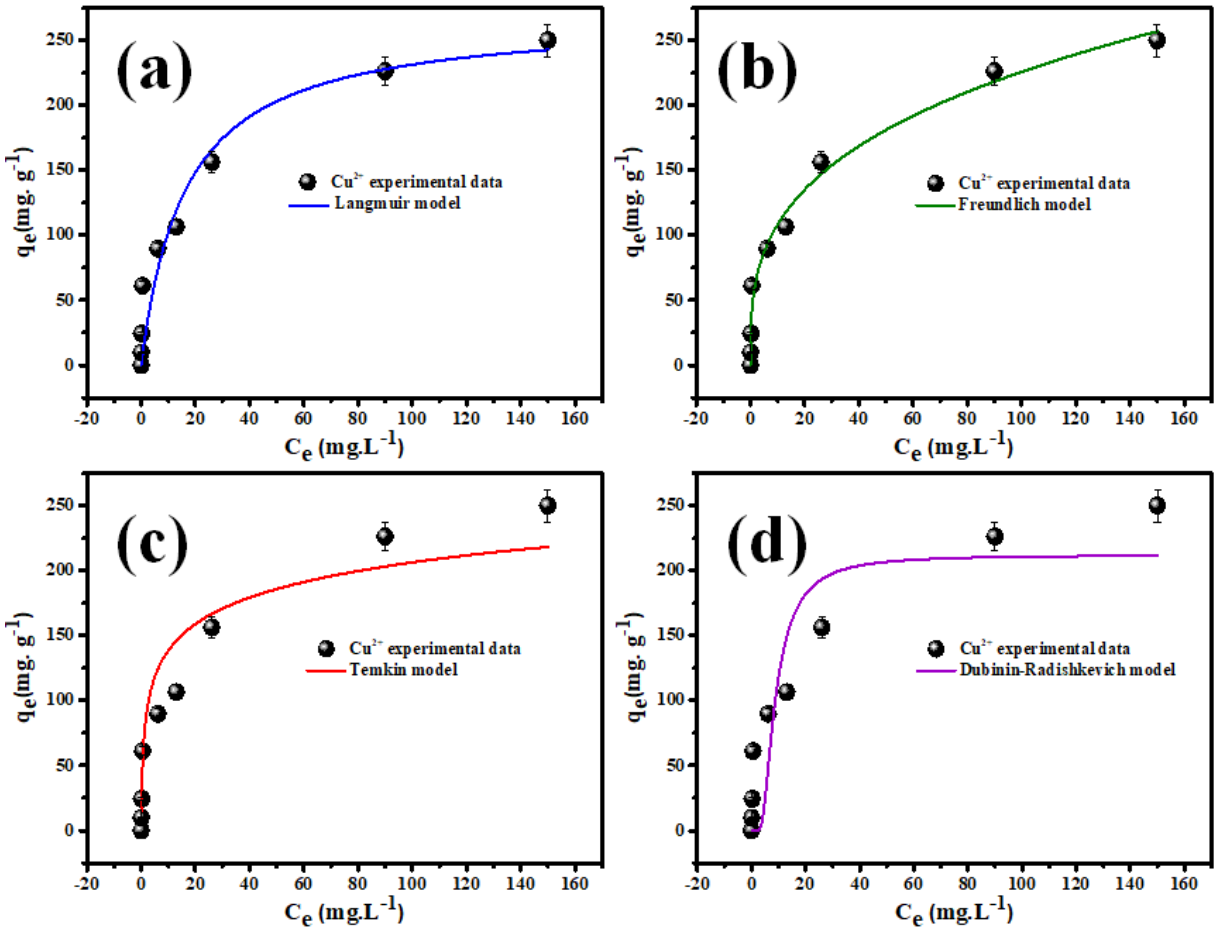

Figure 6. Removal of Cu (II) ions equilibrium data formfitting using non-linear: (**a**) Langmuir; (**b**) Freundlich; (**c**) Temkin; and (**d**) Dubinin-Radushkevich models.

Table 1. Various equilibrium Isotherm constants for Cu (II) adsorption by the nanocomposites MgY_2O_4@g-C_3N_4.

Equilibrium Model	Parameters	Cu^{2+}
Langmuir	qm (mg·g^{-1})	**290.7**
	K_L (mg·g^{-1})	**0.028**
	R_L (L.mg^{-1})	**0.125**
	R^2	**0.9965**
Freundlich	n	**1.48**
	K_F (L.mg^{-1})	**11.36**
	R^2	**0.9644**
Temkin	B (J.mol^{-1})	**85.65**
	K_T (L.mg^{-1})	**5.46**
	R^2	**0.9302**
Dubinin-Radushkevich	β (mol^2.J^{-2})	**2.0.95 × 10^{-8}**
	q (mg·g^{-1})	**186.32**
	E (J.mol^{-1})	**4886.5**
	R^2	**0.9833**

3.2.5. Adsorption Kinetics Modeling

Formula (7) illustrates the Lagergren PFO kinetics model with k_1 (1/min) rate constant and q_e is the highest quantity of Cu (II) ions eliminated at equilibrium. Regarding the PSO law (Formula (8)), k_2 represents the rate constant (g/mg·min) and the initial sorption rate (h_0) can be determined by $h_0 = k_2.qe$. The half-life time, $t_{1/2} = 1/(k_2.q_{e2})$, is the time period over which Cu (II) metal ions are eliminated at half the equilibrium concentration of metal ions [47]. For the IPD mechanism model (Formula (10)), the parameters C that provides the thickness of boundary layer is obtained from the intercept, while the rate constant k_{dif1} (in mg/g·min$^{1/2}$), is computed from the graph's slope (Figure 7). A regression coefficient R^2 is applied to test the validity of these models. Table 2 shows variables estimated from the analysis of measured Cu (II) sorption values by kinetic models. It is apparent that the PSO model perfectly models the kinetics data of Cu (II) adsorption on MgY_2O_4@g-C_3N_4 nanomaterials since the R^2 is 0.9978, indicating the presence of chemisorption supporting the Langmuir mode of adsorption [46]. Moreover, the computed quantity of q_e = 86.88 mg/g is an exact match to the determined quantity of q_e = 86.88 mg/g. Therefore, according to the literature, the PSO model can be employed to forecast the adsorption of metals ion on activated carbon [48]. The PSO kinetics model can be utilized to determine entire steps of the adsorption progression, such as outer film diffusion, adsorption, and internal particle diffusion [49]. Furthermore, the experimental data have been simulated by the Elovich by q_t vs. t graph (Figure 7), where the initial rate a and β values were derived from the intercept and the slope, respectively. The parameters α and β are the initial sorption rate constant (mg/g min) and the extent of surface coverage and the activation energy for chemisorption (g/mg). The data fitting to the Elovich model is indicated by the R^2 (i.e., 0.9422) [50]. The relative matching with the Elovich equation corroborates a chemisorption control on the adsorption process in agreement with the PSO kinetic model [50,51].

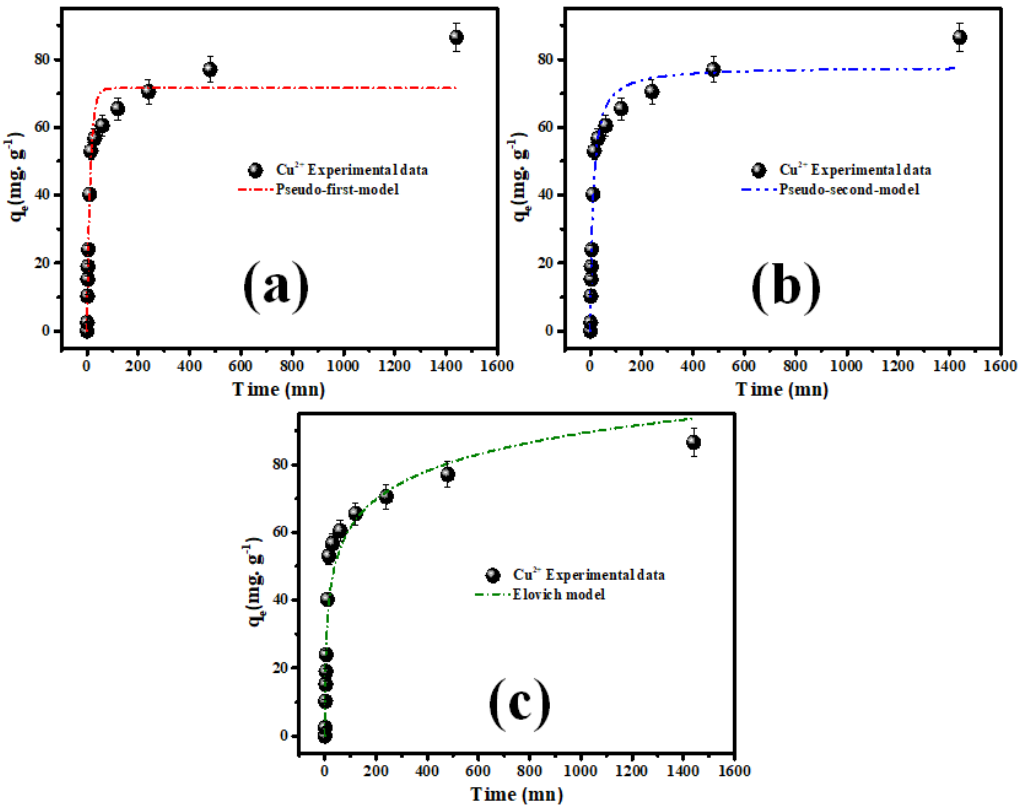

Figure 7. Nonlinear graphs: (**a**) PFO; (**b**) PSO; and (**c**) Elovich kinetics models for Cu (II) ions adsorption onto the fabricated MgY_2O_4@g-C_3N_4 nanomaterials.

Table 2. Calculated kinetic model parameters for Cu (II) adsorption on MgY_2O_4@g-C_3N_4 nanomaterials.

	Pseudo-Second-Order Model					
Cu^{2+}	$q_{e(Exp)}$ ($mg \cdot g^{-1}$)	$t_{1/2}$ (min)	h_0 ($mg \cdot g^{-1} \cdot min^{-1}$)	$q_{e(Cal)}$ ($mg \cdot g^{-1}$)	$K_2 \times 10^4$ ($g \cdot mg^{-1} \cdot min^{-1}$)	r^2
	89.75 ± 1.57	24.31 ± 0.86	3.57 ± 0.12	86.88 ± 1.23	4.73 ± 0.23	**0.9978**
	Pseudo-First-order model			**Elovich model**		
	q_e(Cal) ($mg \cdot g^{-1}$)	$K_1 \times 10^3$ (min^{-1})	r^2	$\beta \times 10^2$ ($g \cdot mg^{-1}$)	α	r^2
Cu^{2+}	**37.66 ± 1.98**	**2.31 ± 0.18**	**0.9378**	**8.38 ± 0.18**	**21.52 ± 1.26**	**0.9422**

Consequently, the data from the kinetics experiment were evaluated with the intraparticle diffusion kinetic model (Figure 8). Numerous studies have shown that the intraparticle diffusion graph may exhibit multi-linearity, indicating that multiple steps may occur in the course of the adsorption process [52]. The results suggest that the majority of data points fall within two straight lines, as shown in Figure 8. The k_{dif2} estimate for the MgY_2O_4@g-C_3N_4 nanomaterials is less than the k_{dif1} value nominates the intra-particle diffusion as the rate-determining step for Cu (II) adsorption onto the nanomaterials fabricated. In addition, it is essential to note that the slight deviation of the straight lines at the beginning suggests that intra-particle diffusion may not be the only rate-limiting step in the adsorption of Cu (II) ions onto MgY_2O_4@g-C_3N_4 nanomaterials; additional probable surface adsorption processes are involved in the overall sorption rate also [53,54]. Additionally, it is significant to point out that the small deviation of the straight lines indicates that intra-particle diffusion might not be the only factor inhibiting the adsorption of Cu (II) on nanomaterials.

Intra-Particle Diffusion/Transport Model					
k_{dif} ($mg \cdot g^{-1} \cdot min^{-1/2}$)	C1	r^2	k_{dif} ($mg \cdot g^{-1} \cdot min^{-1/2}$)	C2	r^2
17.33	**14.81**	**0.9987**	**1.30**	**49.78**	**0.9804**

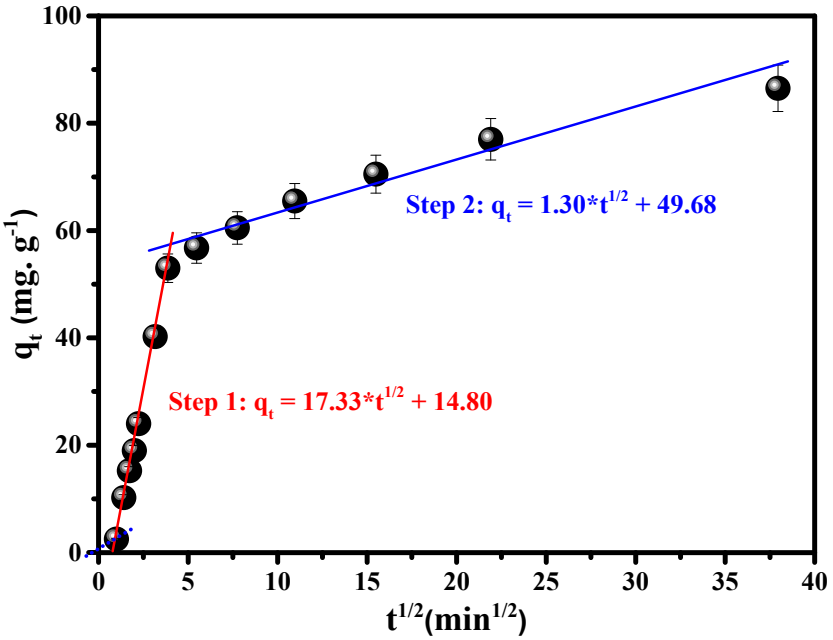

Figure 8. Intra-particle diffusion models (IPD) for Cu ions adsorption onto the prepared MgY_2O_4@g-C_3N_4 nanomaterials.

3.3. Mechanism of Cu (II) Adsorption onto MgY_2O_4@g-C_3N_4 Nanomaterial

The MgY_2O_4@g-C_3N_4 FT-IR spectrum is depicted in Figure 9a. The spectrum exhibits broad and weak peaks at 3030—3300 cm^{-1}, attributed to the N-H stretches and indicate the hydrogen attachment to the nitrogen atoms [55,56]. The peak located at 2168 cm^{-1} corresponds to C≡N, but the sharp peak at 804 cm^{-1} is belonging to the heptazine ring. The broad peaks in the 900 and 1800 cm^{-1} range are indicative of s-triazine derivatives. The 1445 cm^{-1} stretches can be allocated to the triazine ring (C_3N_3), whereas the maxima at 1316 and 1638 cm^{-1} come from heptazine (C_6N_7) units [17]. The g-C_3N_4 is a graphitic combination of C_3N_3 and C_6N_7 units, according to the FTIR spectrum analysis [57]. Cu (II) adsorption on MgY_2O_4@g-C_3N_4 nanomaterials was identified by FTIR analysis. The FTIR spectra of MgY_2O_4@g-C_3N_4 nanomaterials after Cu (II) adsorption is shown in Figure 9b. After adsorption, the stretching peaks of the O-H and ending amino groups are at lower frequencies. Meanwhile, the peak of the triazine ring mode shifts slightly to 895 cm^{-1} from 885 cm^{-1}. Further, both 561 and 668 cm^{-1} stretching vibration patterns [7,58] have substantially turned orientation, showing a reaction between Cu (II) and oxygen atoms of MgY_2O_4 by π-π stacking bridge. The findings suggest that functional groups of MgY_2O_4@g-C_3N_4 (OH, CN, and N-H) and p electron distributions of the triazine ring (C_3N_3) may be responsible for the binding of the Cu (II) ions to the adsorbent surface through a chemisorption route. A study by (FTIR) demonstrated that the triazine ring functions as a Lewis base and aids in the Cu (II) elimination process, as proven by FTIR investigations. Figure 9b depicts a possible adsorption pathway for Cu (II) onto MgY_2O_4@g-C_3N_4 relying on the FTIR measurements described above.

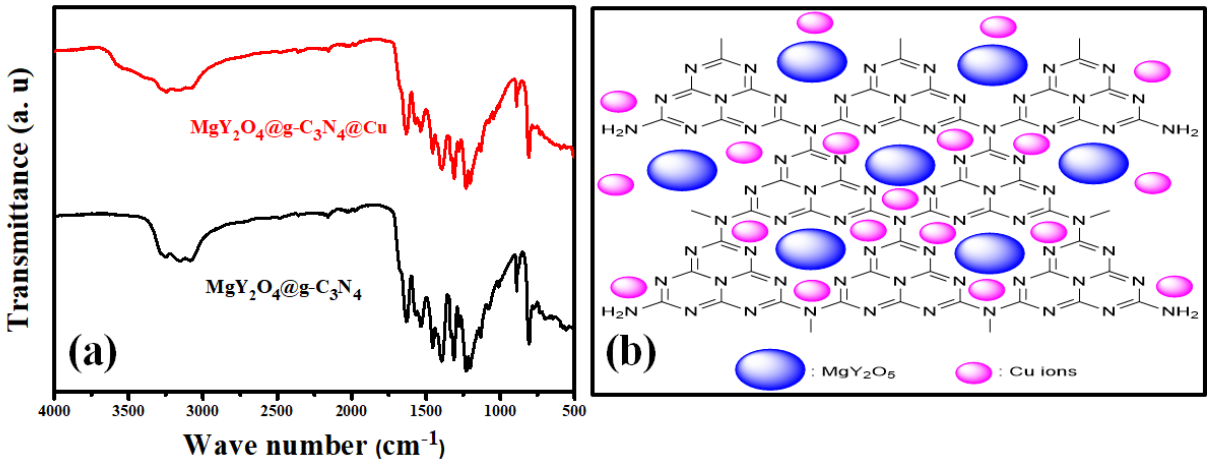

Figure 9. (**a**) FTIR spectra of MgY_2O_4@g-C_3N_4 nanomaterials previously and after Cu (II) adsorption; and (**b**) proposed adsorption mechanism.

Consistent with the data in Table 3, the adsorption tendency of MgY_2O_4@g-C_3N_4 nanomaterials towards aqueous Cu (II) was further evaluated and compared to different adsorbents that have been reported in the relevant literature. MgY_2O_4@g-C_3N_4 nanomaterial removes Cu (II) from an aqueous solution quickly because it takes less time to reach equilibrium, which is only 40 min. Also, the hetero-nanostructure of the nanomaterials has a higher adsorption capacity than other nanostructures, at 290.7 mg/g compared to 7.4–150 mg/g for other nanostructures used. The high performance of MgY_2O_4@g-C_3N_4 for removing Cu (II) is due to its remarkable nanostructure possessing high porosity. These findings make it a good and potentially competent adsorbent for abolishing various heavy metal ions in the aquatic phase. This behavior is similar that what obtained with Yang and his coworkers in the case of the amino modification of biochar for enhanced adsorption of copper ions from synthetic wastewater [54].

Table 3. Comparison of MgY_2O_4@g-C_3N_4 adsorption parameters with various adsorbents.

Adsorbents Used	Removal Capacity (mg/g)	Refs.
Alg + CNC	53.4	[59]
CNC/Sulfate ($-SO_3^-$)	17.9	[60]
CNF/Tempo	49	[60]
MWCNTs/Chitosan nanocomposite	12.12	[61]
Corn straw	12.5	[62]
Sewage sludge	10.6	[63]
Hardwood	7.4	[64]
Pristine biochar (saw dust char)	16.1	[65]
Spartina alternifora	48.5	[66]
GO/PEI	150.9	[67]
Fe_3O_4@SiO_2@TiO_2-APTMS	50.5	[68]
MgY_2O_4@g-C_3N_4	290.7	Current study

3.4. Reusability and Stability

The multiple uses of an adsorbent are considered by users to be of crucial importance in order to reduce wastewater management expenses and to limit the significant consumption of these adsorbents. To this end, a fairly extensive study through the succession of four adsorption cycles using the same MgY_2O_4@g-C_3N_4 nanomaterials. The results presented in Figure 10 show that the percentage of degradation decreased slightly by less than 10% between the first and the fourth cycle. This decrease is mainly caused by a negligible saturation of the microporous part of MgY_2O_4@g-C_3N_4 nanomaterials. This study confirms that MgY_2O_4@g-C_3N_4 nanomaterials could be effectively reused for the treatment of wastewater loaded with mineral pollution. Likewise, this slight decrease is considered negligible because most industrial adsorbents have a lifespan of a few months after we note a saturation of the pores with a difficulty in desorption.

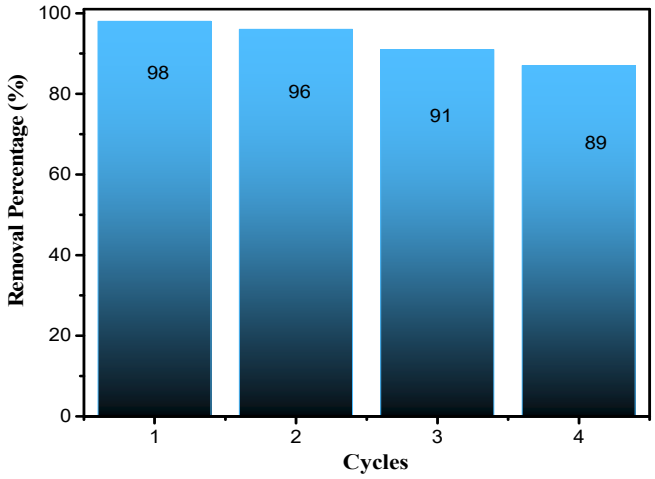

Figure 10. Variation of removal percentage of Cu (II) using MgY_2O_4@g-C_3N_4 nanomaterials.

A sorbent with an interesting absorption capacity and an easy regeneration capability will be selected for other applications with real effluents (pharmaceutical, agricultural and textile effluents). This behavior is similar that obtained by with Yang and his coworkers in the case of the amino modification of biochar for enhanced adsorption of copper ions from synthetic wastewater [51].

An economic analysis for the MgY_2O_4@g-C_3N_4 can be considered from different aspects. The adsorbent is prepared of the graphitic carbon nitride (g-C_3N_4) which is feasibly synthesized from the most earth-abundant elements (carbon and nitrogen) to make strong covalent bonds in its conjugated layer structure and is bonded with the cheap precursors Y_2O_3 and MgO cheap precursors [69]. In addition, the adsorbent has a high

adsorption capacity of 86.65 mg/g within 49 min and can be efficiently reused for four cycles. The amount of Cu (II) ions can be precipitated at high pH to obtain the hydroxides that can be employed to obtain the high-price copper entities [70].

For industrial-scale applications, the adsorbents can be sealed in a meticulous form by being lodged in an unyielding package, such as a synthetic or natural polymer, to ensure nanomaterial trapping and non-release in the water system. Such a prearrangement can be implemented to shuffle to a fixed-bed column for continuous flow treatment pilots [71].

4. Conclusions

In conclusion, MgY_2O_5@g-C_3N_4 nanomaterials were produced and tested as a Cu (II) adsorbent material in water. The BET and TEM analyses validated the material's nanomaterials morphology. At a pH of 3.0, the MgY_2O_5@g-C_3N_4 nanomaterials displayed outstanding Cu (II) adsorption capability. Cu (II) adsorption on MgY_2O_5@g-C_3N_4 nanomaterials followed the Langmuir isotherm model, with a maximum theoretical adsorption capacity of 290.7 mg/g. Adsorption kinetics suggested that the pseudo-second-order model may be used to describe the adsorption process. An FTIR examination revealed an abundance of hydroxyl groups on the surface of MgY_2O_5@g-C_3N_4 nanomaterials and surface complexation dominated Cu (II) adsorption. MgY_2O_5@g-C_3N_4 nanoparticles have tremendous potential as an adsorbent for removing Cu (II) from an aqueous solution in environmental pollution treatment due to their easy fabrication and high removal capability. Moreover, the results of the reusability analysis showed that the percentage of degradation decreased slightly by less than 10% between the first and the fourth cycle. This decrease is mainly caused by a negligible saturation of the microporous part of MgY_2O_4@g-C_3N_4 nanomaterials. This study confirms that MgY_2O_4@g-C_3N_4 nanomaterials could be effectively reused for the treatment of wastewater loaded with mineral pollution. The behavior of this material should be validated in other real matrices (containing a particle and mineral pollution. This will be the subject of our future investigations.

Author Contributions: Methodology, A.M., H.I. and A.A.A.; Formal analysis, A.A. and M.I.; Investigation, L.K. and A.A.A.; Writing—original draft, A.M. and H.I.; Writing—review & editing, L.K., A.A., A.A.A. and P.N.-T.; Supervision, M.I. and A.A.A. All authors have read and agreed to the published version of the manuscript.

Funding: The authors extend their appreciation to the Deputyship for Research& Innovation, Ministry of Education, Saudi Arabia for funding this research work through the project number (QU-IF-4-5-1-29053).

Acknowledgments: The authors thank to Qassim University for technical support.

Conflicts of Interest: The authors declare no conflict of interest.

References

1. Saravanan, A.; Kumar, P.S.; Ramesh, B.; Srinivasan, S. Removal of toxic heavy metals using genetically engineered microbes: Molecular tools, risk assessment and management strategies. *Chemosphere* **2022**, *298*, 134341. [CrossRef]
2. Mukherjee, A.G.; Wanjari, U.R.; Renu, K.; Vellingiri, B.; Gopalakrishnan, A.V. Heavy metal and metalloid-induced reproductive toxicity. *Environ. Toxicol. Pharmacol.* **2022**, *92*, 103859. [CrossRef] [PubMed]
3. Burnase, N.; Jaiswal, S.; Barapatre, A. Metal Toxicity in Humans Associated with Their Occupational Exposures Due to Mining. In *Medical Geology in Mining: Health Hazards Due to Metal Toxicity*; Springer: Cham, Switzerland, 2022; pp. 127–186. [CrossRef]
4. Xu, R.; Yang, Z.; Niu, Y.; Xu, D.; Wang, J.; Han, J.; Wang, H. Removal of microplastics and attached heavy metals from secondary effluent of wastewater treatment plant using interpenetrating bipolar plate electrocoagulation. *Sep. Purif. Technol.* **2022**, *290*, 120905. [CrossRef]
5. Chakraborty, S.C.; Zaman, W.U.; Hoque, M.; Qamruzzaman; Zaman, J.U.; Hossain, D.; Pramanik, B.K.; Nguyen, L.N.; Nghiem, L.D.; Mofijur; et al. Metals extraction processes from electronic waste: Constraints and opportunities. *Environ. Sci. Pollut. Res.* **2022**, *29*, 32651–32669. [CrossRef]
6. Liaqat, A.; Zahra, I.; Abbas, S.Z.; Wabaidur, S.M.; Eldesoky, G.E.; Islam, A.; Rafatullah, M.; Shakoori, F.R.; Shakoori, A.R. Copper Bioremediation Ability of Ciliate *Paramecium multimicronucleatum* Isolated from Industrial Wastewater. *Water* **2022**, *14*, 1419. [CrossRef]

7. Ismail, M.; Jobara, A.; Bekouche, H.; Allateef, M.A.; Ben Aissa, M.A.; Modwi, A. Impact of Cu Ions removal onto MgO nanostructures: Adsorption capacity and mechanism. *J. Mater. Sci. Mater. Electron.* **2022**, *33*, 12500–12512. [CrossRef]
8. Abaker, Z.; Hussein, T.; Makawi, S.; Mustafa, B.; Modwi, A. Superior uptake of Cu (II) from aquatic media via Y_2O_3-ZnO nanostructures. *Nano-Struct. Nano-Objects* **2022**, *30*, 100879. [CrossRef]
9. Lou, X.-Y.; Boada, R.; Verdugo, V.; Simonelli, L.; Pérez, G.; Valiente, M. Decoupling the adsorption mechanisms of arsenate at molecular level on modified cube-shaped sponge loaded superparamagnetic iron oxide nanoparticles. *J. Environ. Sci.* **2022**, *121*, 1–12. [CrossRef]
10. Khulbe, K.C.; Matsuura, T. Removal of heavy metals and pollutants by membrane adsorption techniques. *Appl. Water Sci.* **2018**, *8*, 19. [CrossRef]
11. Zhang, S.; Li, H.; Wu, Z.; Post, J.E.; Lanson, B.; Liu, Y.; Hu, B.; Wang, M.; Zhang, L.; Hong, M.; et al. Effects of cobalt doping on the reactivity of hausmannite for As(III) oxidation and As(V) adsorption. *J. Environ. Sci.* **2022**, *122*, 217–226. [CrossRef]
12. Zaimee, M.Z.A.; Sarjadi, M.S.; Rahman, L. Heavy Metals Removal from Water by Efficient Adsorbents. *Water* **2021**, *13*, 2659. [CrossRef]
13. Zamora-Ledezma, C.; Negrete-Bolagay, D.; Figueroa, F.; Zamora-Ledezma, E.; Ni, M.; Alexis, F.; Guerrero, V.H. Heavy metal water pollution: A fresh look about hazards, novel and conventional remediation methods. *Environ. Technol. Innov.* **2021**, *22*, 101504. [CrossRef]
14. Lou, X.-Y.; Boada, R.; Simonelli, L.; Valiente, M. Enhanced arsenite removal by superparamagnetic iron oxide nanoparticles in-situ synthesized on a commercial cube-shape sponge: Adsorption-oxidation mechanism. *J. Colloid Interface Sci.* **2022**, *614*, 460–467. [CrossRef]
15. Qi, X.; Tong, X.; Pan, W.; Zeng, Q.; You, S.; Shen, J. Recent advances in polysaccharide-based adsorbents for wastewater treatment. *J. Clean. Prod.* **2021**, *315*, 128221. [CrossRef]
16. Rajasulochana, P.; Preethy, V. Comparison on efficiency of various techniques in treatment of waste and sewage water—A comprehensive review. *Resour. Technol.* **2016**, *2*, 175–184. [CrossRef]
17. Ali, M.; Modwi, A.; Idriss, H.; Aldaghri, O.; Ismail, M.; Ibnaouf, K. Detoxification of Pb (II) from aquatic media via $CaMgO_2$@g-C_3N_4 nanocomposite. *Mater. Lett.* **2022**, *322*, 132501. [CrossRef]
18. Nair, R.R.; Mary, B.C.J.; Vijaya, J.J.; Mustafa, A.; Khezami, L.; Modwi, A.; Ismail, M.; Bououdina, M.; Lemine, O.M. Reduced graphene oxide/spinel ferrite nanocomposite as an efficient adsorbent for the removal of Pb (II) from aqueous solution. *J. Mater. Sci. Mater. Electron.* **2021**, *32*, 28253–28274. [CrossRef]
19. Idriss, H.; Alakhras, A.; El Khair, H. Malachite green removal from aqueous solutions by MgO (86%). Se (7%). Te (7%) nanocomposites. *Chalcogenide Lett.* **2021**, *18*, 629–638. [CrossRef]
20. Khezami, L.; Ben Aissa, M.A.; Modwi, A.; Ismail, M.; Guesmi, A.; Algethami, F.K.; Ben Ticha, M.; Assadi, A.A.; Nguyen-Tri, P. Harmonizing the photocatalytic activity of g-C_3N_4 nanosheets by ZrO_2 stuffing: From fabrication to experimental study for the wastewater treatment. *Biochem. Eng. J.* **2022**, *182*, 108411. [CrossRef]
21. Idriss, H. Decolorization of malachite green in aqueous solution via MgO nanopowder. *J. Optoelectron. Biomed. Mater.* **2021**, *13*, 183–192. [CrossRef]
22. Ben Aissa, M.A.; Khezami, L.; Taha, K.; Elamin, N.; Mustafa, B.; Al-Ayed, A.S.; Modwi, A. Yttrium oxide-doped ZnO for effective adsorption of basic fuchsin dye: Equilibrium, kinetics, and mechanism studies. *Int. J. Environ. Sci. Technol.* **2021**, *19*, 9901–9914. [CrossRef]
23. Modwi, A.; Khezami, L.; Ghoniem, M.G.; Nguyen-Tri, P.; Baaloudj, O.; Guesmi, A.; AlGethami, F.K.; Amer, M.S.; Assadi, A.A. Superior removal of dyes by mesoporous MgO/g-C_3N_4 fabricated through ultrasound method: Adsorption mechanism and process modeling. *Environ. Res.* **2022**, *205*, 112543. [CrossRef] [PubMed]
24. Toghan, A.; Abd El-Lateef, H.M.; Taha, K.K.; Modwi, A. Mesoporous TiO_2@g-C_3N_4 composite: Construction, characterization, and boosting indigo carmine dye destruction. *Diam. Relat. Mater.* **2021**, *118*, 108491. [CrossRef]
25. Osorio-Vargas, P.; Pais-Ospina, D.; Marin-Silva, D.A.; Pinotti, A.; Damonte, L.; Cánneva, A.; Donadelli, J.A.; da Costa, L.P.; Pizzio, L.R.; Torres, C.C.; et al. TiO_2 nanorods doped with g-C_3N_4—Polyethylene composite coating for self-cleaning applications. *Mater. Chem. Phys.* **2022**, *288*, 126356. [CrossRef]
26. Reddy, K.R.; Reddy, C.V.; Nadagouda, M.N.; Shetti, N.P.; Jaesool, S.; Aminabhavi, T.M. Polymeric graphitic carbon nitride (g-C_3N_4)-based semiconducting nanostructured materials: Synthesis methods, properties and photocatalytic applications. *J. Environ. Manag.* **2019**, *238*, 25–40. [CrossRef]
27. Al-Jabari, M.H.; Sulaiman, S.; Ali, S.; Barakat, R.; Mubarak, A.; Khan, S.A. Adsorption study of levofloxacin on reusable magnetic nanoparticles: Kinetics and antibacterial activity. *J. Mol. Liq.* **2019**, *291*, 111249. [CrossRef]
28. Langmuir, I. The adsorption of gases on plane surfaces of glass, mica and platinum. *J. Am. Chem. Soc.* **1918**, *40*, 1361–1403. [CrossRef]
29. Hu, Q.; Zhang, Z. Application of Dubinin–Radushkevich isotherm model at the solid/solution interface: A theoretical analysis. *J. Mol. Liq.* **2019**, *277*, 646–648. [CrossRef]
30. Temkin, M.I. Adsorption equilibrium and the kinetics of processes on nonhomogeneous surfaces and in the interaction between adsorbed molecules. *Zh. Fiz. Chim.* **1941**, *15*, 296–332.

31. Ghorbani, M.; Ariavand, S.; Aghamohammadhasan, M.; Seyedin, O. Synthesis and optimization of a green and efficient sorbent for removal of three heavy metal ions from wastewater samples: Kinetic, thermodynamic, and isotherm studies. *J. Iran. Chem. Soc.* **2021**, *18*, 1947–1963. [CrossRef]
32. Yu, Y.; Yan, W.; Wang, X.; Li, P.; Gao, W.; Zou, H.; Wu, S.; Ding, K. Surface engineering for extremely enhanced charge separation and photocatalytic hydrogen evolution on g-C_3N_4. *Adv. Mater.* **2018**, *30*, 1705060. [CrossRef] [PubMed]
33. Vesali-Kermani, E.; Habibi-Yangjeh, A.; Ghosh, S. Visible-light-induced nitrogen photofixation ability of g-C_3N_4 nanosheets decorated with MgO nanoparticles. *J. Ind. Eng. Chem.* **2020**, *84*, 185–195. [CrossRef]
34. Chen, G.; Lei, R.; Wang, H.; Huang, F.; Zhao, S.; Xu, S. Temperature-dependent emission color and temperature sensing behavior in Tm^{3+}/Yb^{3+}: Y_2O_3 nanoparticles. *Opt. Mater.* **2018**, *77*, 233–239. [CrossRef]
35. Sotomayor, F.J.; Cychosz, K.A.; Thommes, M. Characterization of micro/mesoporous materials by physisorption: Concepts and case studies. *Acc. Mater. Surf. Res* **2018**, *3*, 34–50.
36. Tran, C.V.; Quang, D.V.; Nguyen Thi, H.P.; Truong, T.N.; La, D.D. Effective removal of Pb (II) from aqueous media by a new design of Cu–Mg binary ferrite. *ACS Omega* **2020**, *5*, 7298–7306. [CrossRef]
37. Mao, N.; Jiang, J.-X. MgO/g-C_3N_4 nanocomposites as efficient water splitting photocatalysts under visible light irradiation. *Appl. Surf. Sci.* **2019**, *476*, 144–150. [CrossRef]
38. van der Heide, P. Photoelectron binding energy shifts observed during oxidation of group IIA, IIIA and IVA elemental surfaces. *J. Electron Spectrosc. Relat. Phenom.* **2006**, *151*, 79–91. [CrossRef]
39. Pan, T.-M.; Lee, J.-D. Physical and Electrical Properties of Yttrium Oxide Gate Dielectrics on Si Substrate with NH_3 Plasma Treatment. *J. Electrochem. Soc.* **2007**, *154*, H698–H703. [CrossRef]
40. Amer, M.S.; Arunachalam, P.; Al-Mayouf, A.M.; Prasad, S.; Alshalwi, M.N.; Ghanem, M.A. Mesoporous Tungsten Trioxide Photoanodes Modified with Nitrogen-Doped Carbon Quantum Dots for Enhanced Oxygen Evolution Photo-Reaction. *Nanomaterials* **2019**, *9*, 1502. [CrossRef]
41. He, Y.; Wang, Y.; Zhang, L.; Teng, B.; Fan, M. High-efficiency conversion of CO_2 to fuel over ZnO/g-C_3N_4 photocatalyst. *Appl. Catal. B Environ.* **2015**, *168*, 1–8. [CrossRef]
42. Sun, Q.; Lv, K.; Zhang, Z.; Li, M.; Li, B. Effect of contact interface between TiO_2 and g-C_3N_4 on the photoreactivity of g-C_3N_4/TiO_2 photocatalyst: (0 0 1) vs (1 0 1) facets of TiO_2. *Appl. Catal. B Environ.* **2015**, *164*, 420–427.
43. Hamdy, A. Experimental study of the relationship between dissolved iron, turbidity, and removal of Cu (II) ion from aqueous solutions using zero-valent iron nanoparticles. *Arab. J. Sci. Eng.* **2021**, *46*, 5543–5565. [CrossRef]
44. Zhu, S.; Xu, J.; Wang, B.; Xie, J.; Ying, G.; Li, J.; Cheng, Z.; Li, J.; Chen, K. Highly efficient and rapid purification of organic dye wastewater using lignin-derived hierarchical porous carbon. *J. Colloid Interface Sci.* **2022**, *625*, 158–168. [CrossRef]
45. Biswas, M.C.; Chowdhury, A.; Hossain, M. Applications, drawbacks, and future scope of nanoparticle-based polymer composites. In *Nanoparticle-Based Polymer Composites*; Elsevier: Amsterdam, The Netherlands, 2022; pp. 243–275. [CrossRef]
46. García-Diéguez, M.; Hibbitts, D.D.; Iglesia, E. Hydrogen Chemisorption Isotherms on Platinum Particles at Catalytic Temperatures: Langmuir and Two-Dimensional Gas Models Revisited. *J. Phys. Chem. C* **2019**, *123*, 8447–8462. [CrossRef]
47. Baaloudj, O.; Nasrallah, N.; Kebir, M.; Guedioura, B.; Amrane, A.; Nguyen-Tri, P.; Nanda, S.; Assadi, A.A. Artificial neural network modeling of cefixime photodegradation by synthesized $CoBi_2O_4$ nanoparticles. *Environ. Sci. Pollut. Res.* **2021**, *28*, 15436–15452. [CrossRef]
48. Karri, R.R.; Sahu, J. Modeling and optimization by particle swarm embedded neural network for adsorption of zinc (II) by palm kernel shell based activated carbon from aqueous environment. *J. Environ. Manag.* **2018**, *206*, 178–191. [CrossRef]
49. Charaabi, S.; Absi, R.; Pensé-Lhéritier, A.-M.; Le Borgne, M.; Issa, S. Adsorption studies of benzophenone-3 onto clay minerals and organosilicates: Kinetics and modelling. *Appl. Clay Sci.* **2021**, *202*, 105937. [CrossRef]
50. Modwi, A.; Khezami, L.; Taha, K.; Al-Duaij, O.; Houas, A. Fast and high efficiency adsorption of Pb(II) ions by Cu/ZnO composite. *Mater. Lett.* **2017**, *195*, 41–44. [CrossRef]
51. Khezami, L.; Taha, K.K.; Modwi, A. Efficient Removal of Cobalt from Aqueous Solution by Zinc Oxide Nanoparticles: Kinetic and Thermodynamic Studies. *Z. Für Nat. A* **2017**, *72*, 409–418. [CrossRef]
52. Usman, A.R.; Sallam, A.S.; Al-Omran, A.; El-Naggar, A.H.; Alenazi, K.K.; Nadeem, M.; Al-Wabel, M.I. Chemically Modified Biochar Produced from Conocarpus Wastes: An Efficient Sorbent for Fe(II) Removal from Acidic Aqueous Solutions. *Adsorpt. Sci. Technol.* **2013**, *31*, 625–640. [CrossRef]
53. Kołodyńska, D.; Wnętrzak, R.; Leahy, J.; Hayes, M.; Kwapiński, W.; Hubicki, Z. Kinetic and adsorptive characterization of biochar in metal ions removal. *Chem. Eng. J.* **2012**, *197*, 295–305. [CrossRef]
54. Usman, A.; Sallam, A.; Zhang, M.; Vithanage, M.; Ahmad, M.; Al-Farraj, A.; Ok, Y.S.; Abduljabbar, A.; Al-Wabel, M. Sorption Process of Date Palm Biochar for Aqueous Cd (II) Removal: Efficiency and Mechanisms. *Water Air Soil Pollut.* **2016**, *227*, 449. [CrossRef]
55. Gibson, K.; Glaser, J.; Milke, E.; Marzini, M.; Tragl, S.; Binnewies, M.; Mayer, H.A.; Meyer, H.-J. Preparation of carbon nitride materials by polycondensation of the single-source precursor aminodichlorotriazine (ADCT). *Mater. Chem. Phys.* **2008**, *112*, 52–56. [CrossRef]
56. Shen, C.; Chen, C.; Wen, T.; Zhao, Z.; Wang, X.; Xu, A. Superior adsorption capacity of g-C_3N_4 for heavy metal ions from aqueous solutions. *J. Colloid Interface Sci.* **2015**, *456*, 7–14. [CrossRef]

57. Cui, Y.; Zhang, J.; Zhang, G.; Huang, J.; Liu, P.; Antonietti, M.; Wang, X. Synthesis of bulk and nanoporous carbon nitride polymers from ammonium thiocyanate for photocatalytic hydrogen evolution. *J. Mater. Chem.* **2011**, *21*, 13032–13039. [CrossRef]
58. Feng, Y.; Chen, G.; Zhang, Y.; Li, D.; Ling, C.; Wang, Q.; Liu, G. Superhigh co-adsorption of tetracycline and copper by the ultrathin g-C_3N_4 modified graphene oxide hydrogels. *J. Hazard. Mater.* **2021**, *424*, 127362. [CrossRef]
59. Abou-Zeid, R.E.; Ali, K.A.; Gawad, R.M.; Kamal, K.H.; Kamel, S.; Khiari, R. Removal of Cu (II), Pb (II), Mg (II), and Fe (II) by adsorption onto alginate/nanocellulose beads as bio-sorbent. *J. Renew. Mater.* **2021**, *9*, 601. [CrossRef]
60. Azzaz, A.A.; Jellali, S.; Akrout, H.; Assadi, A.A.; Bousselmi, L. Dynamic investigations on cationic dye desorption from chemically modified lignocellulosic material using a low-cost eluent: Dye recovery and anodic oxidation efficiencies of the desorbed solutions. *J. Clean. Prod.* **2018**, *201*, 28–38. [CrossRef]
61. Eldeeb, T.M.; El Nemr, A.; Khedr, M.H.; El-Dek, S.I. Efficient removal of Cu(II) from water solution using magnetic chitosan nanocomposite. *Nanotechnol. Environ. Eng.* **2021**, *6*, 34. [CrossRef]
62. Chen, X.; Chen, G.; Chen, L.; Chen, Y.; Lehmann, J.; McBride, M.B.; Hay, A.G. Adsorption of copper and zinc by biochars produced from pyrolysis of hardwood and corn straw in aqueous solution. *Bioresour. Technol.* **2011**, *102*, 8877–8884. [CrossRef]
63. Wang, X.; Liang, X.; Wang, Y.; Wang, X.; Liu, M.; Yin, D.; Xia, S.; Zhao, J.; Zhang, Y. Adsorption of Copper (II) onto activated carbons from sewage sludge by microwave-induced phosphoric acid and zinc chloride activation. *Desalination* **2011**, *278*, 231–237. [CrossRef]
64. Han, Y.; Boateng, A.A.; Qi, P.X.; Lima, I.M.; Chang, J. Heavy metal and phenol adsorptive properties of biochars from pyrolyzed switchgrass and woody biomass in correlation with surface properties. *J. Environ. Manag.* **2013**, *118*, 196–204. [CrossRef] [PubMed]
65. Yang, G.-X.; Jiang, H. Amino modification of biochar for enhanced adsorption of copper ions from synthetic wastewater. *Water Res.* **2014**, *48*, 396–405. [CrossRef]
66. Xiao, F.; Cheng, J.; Cao, W.; Yang, C.; Chen, J.; Luo, Z. Removal of heavy metals from aqueous solution using chitosan-combined magnetic biochars. *J. Colloid Interface Sci.* **2019**, *540*, 579–584. [CrossRef] [PubMed]
67. Kuang, Y.; Zhang, Z.; Wu, D. Synthesis of graphene oxide/polyethyleneimine sponge and its performance in the sustainable removal of Cu(II) from water. *Sci. Total. Environ.* **2021**, *806*, 151258. [CrossRef] [PubMed]
68. Bilgic, A. Fabrication of monoBODIPY-functionalized Fe_3O_4@ SiO_2@ TiO_2 nanoparticles for the photocatalytic degradation of rhodamine B under UV irradiation and the detection and removal of Cu (II) ions in aqueous solutions. *J. Alloy. Compd.* **2022**, *899*, 163360. [CrossRef]
69. Ismael, M. A review on graphitic carbon nitride (g-C_3N_4) based nanocomposites: Synthesis, categories, and their application in photocatalysis. *J. Alloy. Compd.* **2020**, *846*, 156446. [CrossRef]
70. Meramo-Hurtado, S.I.; González-Delgado, A.D. Application of techno-economic and sensitivity analyses as decision-making tools for assessing emerging large-scale technologies for production of chitosan-based adsorbents. *ACS Omega* **2020**, *5*, 17601–17610. [CrossRef]
71. Aziz, F.; El Achaby, M.; Lissaneddine, A.; Aziz, K.; Ouazzani, N.; Mamouni, R.; Mandi, L. Composites with alginate beads: A novel design of nano-adsorbents impregnation for large-scale continuous flow wastewater treatment pilots. *Saudi J. Biol. Sci.* **2019**, *27*, 2499–2508. [CrossRef] [PubMed]